

In-plane Cr₂N-CrN metal-semiconductor heterostructure with improved thermoelectric properties

Bidesh Biswas ^{1,2} Sourjyadeep Chakraborty ^{1,2} Ongira Chowdhury,³ Dheemahi Rao ^{1,2} Ashalatha Indiradevi Kamalasanan Pillai ⁴ Vijay Bhatia ⁴ Magnus Garbrecht ⁴ Joseph P. Feser,³ and Bivas Saha ^{1,2,5,*}

¹Chemistry and Physics of Materials Unit, Jawaharlal Nehru Centre for Advanced Scientific Research, Bangalore 560064, India

²International Centre for Materials Science, Jawaharlal Nehru Centre for Advanced Scientific Research, Bangalore 560064, India

³Department of Mechanical Engineering, University of Delaware, Newark, Delaware 19716, USA

⁴Australian Centre for Microscopy and Microanalysis, The University of Sydney, Camperdown, New South Wales 2006, Australia

⁵School of Advanced Materials, Jawaharlal Nehru Centre for Advanced Scientific Research, Bangalore 560064, India



(Received 12 August 2021; accepted 2 November 2021; published 22 November 2021)

Epitaxial metal-semiconductor heterostructures with suitable Schottky barrier can lead to high thermoelectric figure-of-merit (zT) due to selective filtering of low-energy electrons as well as reduced thermal conductivity from phonon scattering at the interfaces. Lattice-matched vertical metal-semiconductor multilayer/superlattices as well as metallic nanoparticles embedded inside semiconducting hosts have been studied intensively to explore their thermoelectric properties. However, development of in-plane metal-semiconductor heterostructures and exploration of their physical properties have remained elusive primarily due to the growth and fabrication challenges. In-plane heterostructures are expected to be more suitable for planar integration and should exhibit unique properties. In this work, we demonstrate an in-plane Cr₂N-CrN metal-semiconductor heterostructure that exhibits an improved thermoelectric power factor. The in-plane heterostructure is deposited by controlling the Cr-flux during deposition that leads to an in-plane phase separation between the metallic-Cr₂N and semiconducting CrN grains. Temperature-dependent electrical transport exhibits an Arrhenius-type thermal activation behavior with an activation energy of 70 meV, and an in-plane electrical conductivity that is about two orders of magnitude higher than that of CrN. The Seebeck coefficient also remained moderately large at $-150 \mu\text{V/K}$ at 700K leading to a very large power factor of 2.1 mW/mK^2 at 700 K.

DOI: [10.1103/PhysRevMaterials.5.114605](https://doi.org/10.1103/PhysRevMaterials.5.114605)

I. INTRODUCTION

Epitaxial metal-semiconductor superlattice heterostructures have attracted significant interest in recent years for their potential applications in thermionic emission-based waste-heat-to-electrical energy conversion [1–4], optical hyperbolic metamaterials [5–7], thermal hyperconductivity [8–10], and hot-electron photocatalysis [11,12]. Most demonstrations of metal-semiconductor heterostructure utilize vertical multilayers/superlattices based on epitaxial lattice-matched transition metal nitrides (TMN) such as TiN/(Al,Sc)N and (Hf,Zr)N/ScN [13–15], and rare-earth semimetallic compounds (ErAs, TbAs, etc.) embedded inside a III-V semiconducting matrix such as GaAs or InGaAs [16–18]. The principal development objective of heterostructured metamaterial utilizes the Schottky barrier at the metal-semiconductor interfaces that filters out low-energy electrons resulting in an enhancement of the Seebeck coefficient, which is essential for high-efficiency thermoelectric devices [19–21]. High mobility and short carrier lifetimes in such nanocomposite metamaterials are also used to develop commercial terahertz sources, detectors, and modulators [22,23]. Similarly, inter-

faces in metal-semiconductor heterostructures are found to scatter mid-to-long-wavelength phonons that reduce the thermal conductivity necessary for thermoelectric applications [24,25]. In terms of the optical properties, differences in the signs of the dielectric permittivity of metallic and semiconducting layers in metal-semiconductor heterostructure lead to hyperbolic photonic dispersion for the transverse magnetic (TM) wave, which could be utilized to achieve subwavelength imaging, engineering the photonic densities of states for quantum electronic applications, as well as to demonstrate exotic thermal transport properties such as thermal hyperconductivity [5,8,26].

While vertical metal-semiconductor multilayers/superlattices have been developed over the last several years and are currently researched to harness their properties into practical applications, the development of in-plane metal-semiconductor heterostructure has remained elusive primarily due to the growth challenges. Traditional ultrahigh vacuum growth techniques such as molecular beam epitaxy, magnetron sputtering or chemical vapor deposition, etc. do not provide means to deposit in-plane heterostructure unless the spontaneous decomposition of the deposited materials takes place during the growth process at elevated temperature. Since most of the TMN semiconductors utilized in heterostructure development (e.g. ScN, rocksalt-Al_xSc_{1-x}N) exhibit the stable rocksalt phase [6,26] both at ambient and

*Authors to whom correspondence should be addressed: bsaha@jncasr.ac.in; bivas.mat@gmail.com

elevated growth temperature ($\sim 900^\circ\text{C}$), the development of in-plane heterostructure by means of phase separation has proven difficult. Template growth techniques that utilize porous anodic alumina have been utilized for the growth of oriented nanowires of thermoelectric materials like Bi_2Te_3 and SiGe [27–29]. However, those are not helpful for the TMN depositions due to the requirement of high growth temperature in excess of 700°C .

Recently, an in-plane two-dimensional (2D) heterostructure comprising WSe_2 - WS_2 was realized in which different 2D atomic panels are combined in a single atomic layer for applications as a p - n junction with large rectification, high-mobility field-effect transistor, photovoltaic device, and complementary metal-oxide-semiconductor inverter with large current [30–32]. Similarly, a large light emission efficiency in the in-plane WS_2 - MoS_2 heterostructure, a high photo-detectivity of 10^{13} Jones, and a short response time of sub-100 μs have been observed in the in-plane graphene-thin amorphous carbon heterostructure for the applications in electronic circuits and devices [33,34]. Theoretical and experimental efforts are also underway to design 2D in-plane metal-semiconductor heterojunctions comprising $1\text{T-MoS}_2/2\text{H-MoS}_2$ that should work at the Mott-Schottky limits of metal-semiconductor junctions as their band alignments are insensitive to the interface conditions [35,36]. Apart from the relative ease in the transport measurements, in-plane heterostructure also offers seamless planar integration, which should be useful for their industrial applications.

CrN is a commercial-scale hard coating material that is used for abrasion/wear-resistant drill bits, cutting tools, medical implants, silver-luster decorative coating, and other tribology applications due to its corrosion-resistant high hardness and high-temperature stability [37–41]. In recent years, CrN has also attracted significant interest due to its unusual and unique first-order metal-insulator phase transition at ~ 260 – 280 K that is accompanied by both structural (orthorhombic-to-rocksalt) and magnetic (antiferromagnetic-to-paramagnetic) phase transitions, which makes it a potential material for data storage, memory device, and magnetic and electrical switches [42–45]. In addition, CrN exhibits a high thermoelectric power factor (~ 2 mW/m-K²) due to its low bandgap (~ 0.7 eV), large electron-effective mass and suitable carrier concentrations in the 10^{19} – 10^{20} cm⁻³ range [46–50]. Along with the room temperature rocksalt crystal structure, nitrides of Cr exhibit a secondary hexagonal Cr_2N phase that is metallic in nature. Cr_2N can be obtained in the thin film growth process when deposited with a large metallic Cr flux. Previous research has demonstrated that Cr_2N films are stable in ambient and at elevated temperatures ($\sim 400^\circ\text{C}$) with a hardness of 18.9 GPa and an elastic modulus of 265 GPa [51]. A room temperature electrical resistivity of 70 ± 7 $\mu\Omega$ cm and carrier concentration of 8×10^{22} cm⁻³ was reported in Cr_2N that highlights its excellent metallic properties. Moreover, due to the near-equal negative formation enthalpy [52,53], nitridation of chromium (Cr) at elevated temperature results in the formation of secondary Cr_2N phase in CrN , which could be suitable for in-plane heterostructure growth.

In this work, natural phase separation in chromium nitride is utilized to develop an in-plane Cr_2N - CrN metal-

semiconductor heterostructure with sharp interfaces. The composition and size of the metal-semiconductor grains are controlled by carefully tuning the Cr flux during the magnetron sputtering deposition. Compared to the phase pure CrN , the electrical resistivity in the in-plane heterostructure reduces by about two orders of magnitude while maintaining a moderately high Seebeck coefficient due to the Schottky barrier-mediated electron conduction at the metal-semiconductor interface. A high power factor of 2.1 mW/mK² is achieved at 780 K in the heterostructure, which is 56% higher compared to phase pure CrN . Combined with the high power factor, and moderate thermal conductivity, an improved thermoelectric performance is achieved in the heterostructure.

II. EXPERIMENTAL METHODS

Sample growth: Phase-pure rocksalt CrN thin film and in-plane Cr_2N - CrN heterostructures are deposited by carefully controlling the Cr-flux during magnetron sputtering deposition inside an ultrahigh vacuum chamber at a base pressure of 2×10^{-9} Torr. The detailed growth technique can be found in our previous article [54].

Seebeck coefficient and electrical resistivity measurement: Temperature dependent Seebeck coefficient and electrical resistivity of the films were measured inside the helium atmosphere using a Linseis LSR-3 system equipped with IR heater. The samples were mounted in vertical geometry between the two Platinum electrodes and a temperature gradient of 50 K was applied at one end of the sample using a local heater to measure the Seebeck coefficient value in differential method [Fig. 1(c)].

TEM, TKD, and TDTR analysis: The microstructure of the films is characterized with transmission Kikuchi diffraction (TKD) and high-resolution (scanning) transmission electron microscopy [HR(S)/TEM] and energy-dispersive x-ray spectroscopy (EDS). The HRSTEM images and EDS maps were recorded with an image- and probe-corrected and monochromated FEI Themis-Z 60–300 microscope equipped with a high-brightness XFEG source and Super-X EDS detector system for ultra-high-count rates, operated at 300 kV.

TKD was performed on a ThermoFisher Helios Hydra PFIB using an Oxford Symmetry EBSD detector. Maps were collected at 30 kV with approximately 3.2 nA beam current. A collection speed of 12 ms per point was used and a step size of 10 nm. A pre-tilted holder was used with a tilt angle of -20° , the stage was forward-tilted to 20° to provide an incident beam perpendicular to the sample.

Thermal conductivity measurement: Cross-plane thermal conductivity of the films was measured with time-domain thermoreflectance (TDTR) technique [55–59] [Fig. 1(d)]. Samples were measured in a cryostat under a high vacuum (Janis VPF-700ST) from the 300–700 K temperature range. Aluminum (Al) transducer with a thickness of 95 nm was deposited on the samples using DC magnetron sputtering, with the thickness being determined *in situ* during TDTR using picosecond acoustic reflection from the Al/film interface. A detailed description of these methods is presented in the Supplementary Material (SM) section [60].

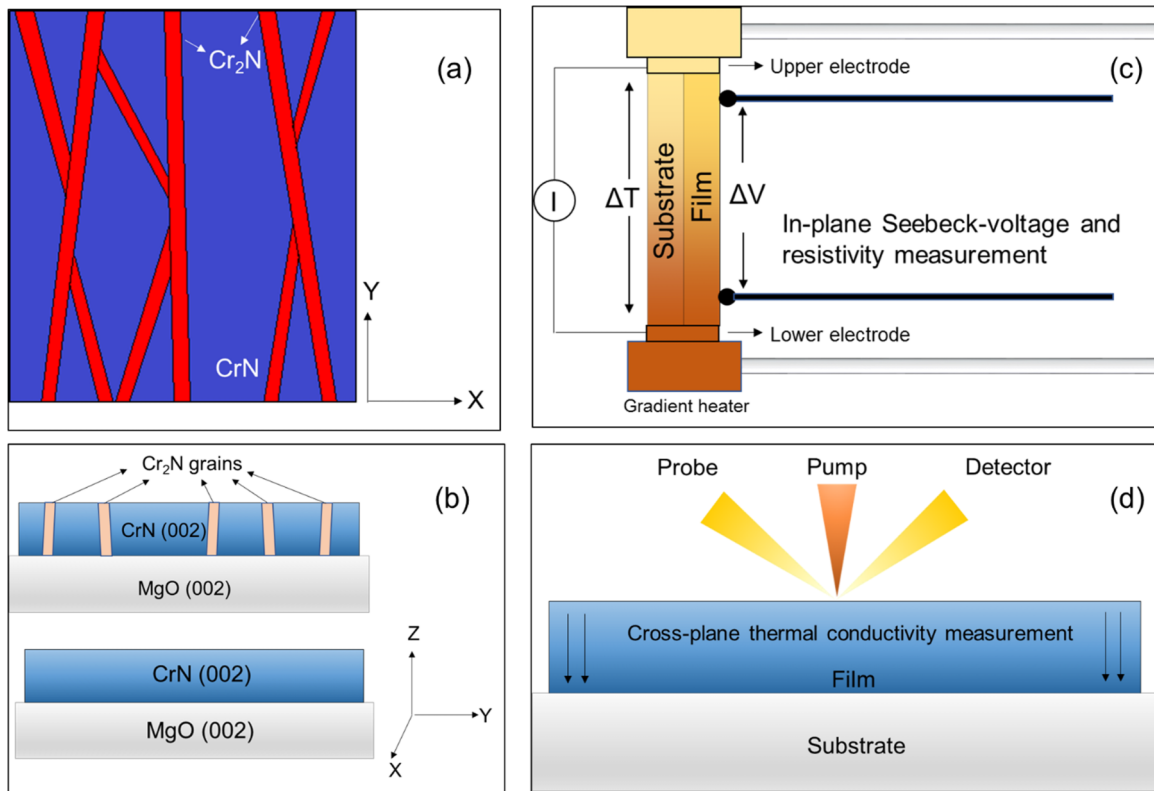


FIG. 1. Schematic diagram of (a) in-plane distribution of Cr₂N and CrN grains in the heterostructure, and (b) side view of the Cr₂N-CrN heterostructure and phase-pure CrN deposited on MgO (002) substrate showing the cross-plane (along z direction) and in-plane (along xy-plane) properties measurement directions. Schematic of the (c) in-plane Seebeck voltage and electrical resistivity measurement setup in Linseis LSR-3 system, and (d) Cross-plane thermal conductivity measurement with TDTR.

III. RESULTS AND DISCUSSION

Band contrast TKD characterization reveals that at low Cr-flux rates during the deposition (growth rate of 1 nm/min), phase-pure, single-crystalline rocksalt semiconducting CrN is obtained. On the other hand, at a high Cr-flux (with a growth rate of 4.16 nm/min), Cr₂N-CrN in-plane heterostructure with interconnected metallic Cr₂N networks is formed (Fig. S1), which results in metal-like in-plane transport properties. On average, the metallic Cr₂N grains occupy 56% of the volume in the heterostructure. At an intermediate Cr flux, resulting in a growth rate 1.83 nm/min, a mixed-phase Cr₂N-CrN in-plane heterostructure is obtained, where the 100–150 nm wide metallic Cr₂N grains are spatially separated by larger semiconducting CrN grains (400–500 nm) and thereby forming an in-plane metal-semiconductor heterostructure [see Fig. 2(a)]. The rocksalt CrN grains grow heteroepitaxially on the (001) MgO substrate due to its close match in lattice parameter and identical crystal structure and extend all the way to the surface of the film, while the Cr₂N grains mostly appear V shaped. The Cr₂N-CrN interface appears abrupt and distinct with a Cr₂N volume fraction of $\sim 17\%$ in the heterostructure. Though CrN has a lower mass density compared to the Cr₂N, higher brightness, and diffraction intensity is an indication of its better crystalline quality and satisfaction of diffraction conditions. The Euler color maps [see Fig. 2(b)] verify the high-quality CrN growth on MgO substrates with identical phase and orientations due to the cubic heteroepitaxy. Pole fig-

ure images [see Fig. 2(c)] for the rocksalt {100} set of planes show that the rocksalt phase grows with the [001] (001) CrN || [001] (001) MgO epitaxial relationship on MgO substrates (with an $\sim 6^\circ$ offset in Fig. 2(c) appearing due to tilt in the sample preparation). Similarly, the pole figure for the {11 $\bar{2}$ 0} set of planes for the hexagonal Cr₂N phase shows that most of the Cr₂N grains are not aligned parallel to the *c* axis of the MgO, but they have multiple orientations. Four orientations are found predominantly, which are oriented approximately 55° away from the Z axis in four different quadrants.

While the TKD analysis establishes the in-plane nature of the heterostructure, HR(S)/TEM analysis is performed to understand the microstructure at the atomic level and to visualize the spatial distribution of different constituent elements of the heterostructure. Low-magnification high-angle annular dark field-scanning transmission electron microscopy (HAADF-STEM) image [see Fig. 3(a)] shows the CrN grains separated by V-shaped metallic Cr₂N grains. Directly at the substrate/film interface, small pyramidal CrN grains are apparent with bright contrast due to strong diffraction conditions. Both the CrN and Cr₂N grains reach the top surface of the film. STEM-EDS maps of different elements [see Figs. 3(b)–3(e)] clearly show the higher Cr concentration in the Cr₂N grains with respect to the stoichiometric 1:1 Cr to N ratio in CrN regions. The boundaries between the Cr₂N and CrN appear atomically sharp [Fig. 3(f)], highlighting the excellent in-plane structural quality of the heterostructure. The corresponding electron diffraction pattern, shown in the

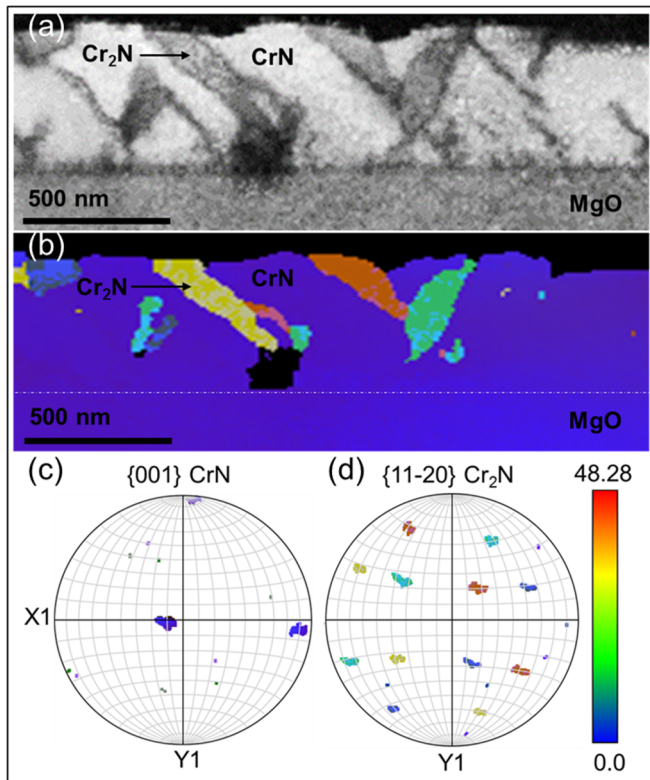


FIG. 2. (a) Band contrast TKD image of the Cr₂N-CrN in-plane metal-semiconductor heterostructure is presented. The CrN grains appear much brighter and larger. The CrN grains are separated by hexagonal Cr₂N along the in-plane direction forming the in-plane heterostructure. (b) Euler color map corresponding to (a), which shows that CrN exhibits the same rocksalt crystal structure and (001) orientation as that of the substrate MgO. Hexagonal Cr₂N grains are not aligned parallel to the *c* axis of rocksalt CrN, as is shown by the pole figures for (c) rocksalt {001} set of planes and (d) hexagonal {11 $\bar{2}$ 0} set of planes.

inset, shows the bright and intense cubic diffraction spots along with weak spots of the hexagonal Cr₂N phase in the out of zone axis. The substrate/film interface appears atomically sharp without interdiffusion of atoms to-and-from the MgO substrate [Fig. 3(g)]. Due to $\sim 1.6\%$ lattice mismatch between the CrN and MgO substrate, a misfit dislocation is visible at the interface.

Thermoelectric transport properties of the phase-pure semiconducting CrN and the in-plane Cr₂N-CrN metal-semiconductor metamaterial along the in-plane direction (Fig. 1 schematic demonstrating the film growth direction and measurement direction of transport properties) is measured in the 300–1000 K temperature range. Resistivity (ρ) of the CrN film is found to decrease with an increase in temperature and exhibits an Arrhenius-type thermal activation due to electron transitions from the valence band to the conduction band at high temperature. At room temperature (300 K), the resistivity of CrN is found to be ~ 138 m Ω cm, which decreases with the rise in temperature and eventually saturates at 2.5 m Ω cm around 800 K, after the onset of the thermal activation. Therefore, compared to the room temperature value, the resistivity decreases by about two orders of magnitude in pure CrN films,

which highlights its excellent semiconducting nature. From the Arrhenius plot ($\ln\rho$ vs $1/T$, see Fig. S6 in the SM [60]) an activation energy of 0.29 eV is determined, which results in an energy gap of 0.58 eV. The measured gap is close to the reported bandgap value of CrN measured with the absorption spectroscopy [50].

Contrary to the phase-pure CrN, the Cr₂N-CrN metal-semiconductor heterostructure exhibits about two orders of magnitude lower resistivity [see Fig. 4(a)]. From 300 to 500 K, the resistivity increases from 1.27 to 1.42 m Ω cm, which is reminiscent of metalliclike conduction. However, after 500 K, resistivity shows a sharp decrease and exhibits a value of ~ 0.96 m Ω cm at ~ 800 K indicating an activation behavior after 500 K. From the Arrhenius-plot (Fig. S6 in the SM [60]) in the 500–800 K region, a barrier height of 70 meV is extracted. The nature of the in-plane resistivity behavior of the heterostructure could be explained by invoking the band structure of the Cr₂N-CrN metal-semiconductor heterostructure, where a Schottky barrier exists between the metallic Cr₂N and semiconducting CrN along the in-plane direction. The measured barrier height represents an averaged Schottky barrier height from all metal-semiconductor interfaces along the in-plane direction (see schematic in Fig. 5). Though the exact origin of the metal-like conductivity at low temperature (< 500 K) remains to be determined, we presume that, at low temperature, electrons do not possess sufficient energy to overcome the Schottky barrier at the interface. However, above 500 K, electrons gain sufficient energy to undergo thermionic emission and/or thermionic field emission that dominates the conduction behavior. The detailed band alignment mechanism [61,62] at the Cr₂N-CrN interface needs further experiments and is beyond the scope of the present study and hence, will be presented subsequently.

The temperature dependent Seebeck coefficient results support the electron transport mechanism in both materials. For phase pure CrN, since the resistivity is large, the overall Seebeck coefficient is also very high [Fig. 4(b)]. With the increase in temperature from 300 to 600 K, the Seebeck coefficient initially increases monotonically from -94 μ V/K to -303 μ V/K. However, on further increase of temperature, the Seebeck coefficient starts to decrease and the overall temperature dependent Seebeck coefficient exhibits a V-shaped curve. Such a V-shaped nature of the Seebeck coefficient is a well-established representation of the thermal activation of carriers in materials [63,64]. Since a large number of carriers participate in the conduction within the thermally activated regime, the Seebeck coefficient decreases at elevated temperatures, which can be also seen from the Mott equation [see Eq. (1)]:

$$S = \frac{8\pi^2 k_B^2 T}{3eh^2} m_s^* \left(\frac{\pi}{3n}\right)^{2/3}, \quad (1)$$

where S is the Seebeck coefficient, n is the carrier concentration, m_s^* is the carrier effective mass, k_B is the Boltzmann constant, and e is the charge of an electron. The manifestation of such thermal activation behavior of carriers, however, is quite stark in semiconducting CrN that highlights not only its superior material quality but also its electronic bandgap with limited defects concentration.

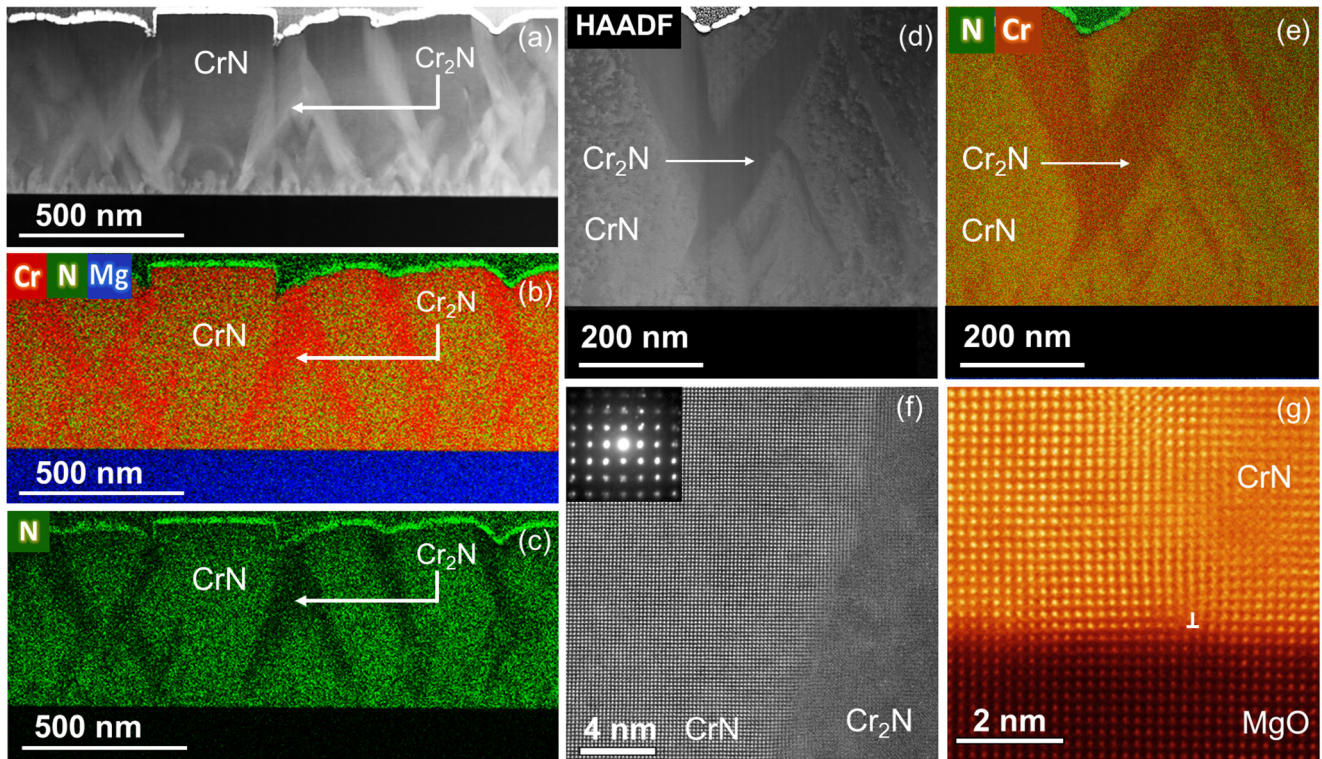


FIG. 3. (a) Low-magnification HAADF-STEM micrograph of the Cr₂N-CrN in-plane heterostructure is presented. At low magnifications, the regions with dark contrast are found to be rocksalt CrN and are separated by bright contrast Cr₂N regions. The corresponding combined STEM-EDS elemental map (b) and individual N map (c) highlight the distinct CrN and Cr₂N grains. (d) A vertical Cr₂N region is presented along with the Cr and N elemental STEM-EDS map in (e). (f) High-resolution HAADF-STEM image showing atomically sharp and abrupt CrN-Cr₂N interface. Electron diffraction pattern (inset) of the heterostructure shows weak diffraction spots of hexagonal Cr₂N (not in zone axis) along with dominant diffraction peaks of cubic CrN (g) Atomic resolution HAADF-STEM image of CrN/MgO interface demonstrates the cubic heteroepitaxial quality of growth. A misfit dislocation is visible due to the slight lattice mismatch.

The Seebeck coefficient of the Cr₂N-CrN metal-semiconductor heterostructure mirrors the nature of phase-pure CrN albeit much less pronounced [Fig. 4(b)].

The values of the Seebeck coefficient of the heterostructure are much lower as compared to the phase-pure CrN. At room temperature (300 K), the in-plane Cr₂N-CrN heterostructure

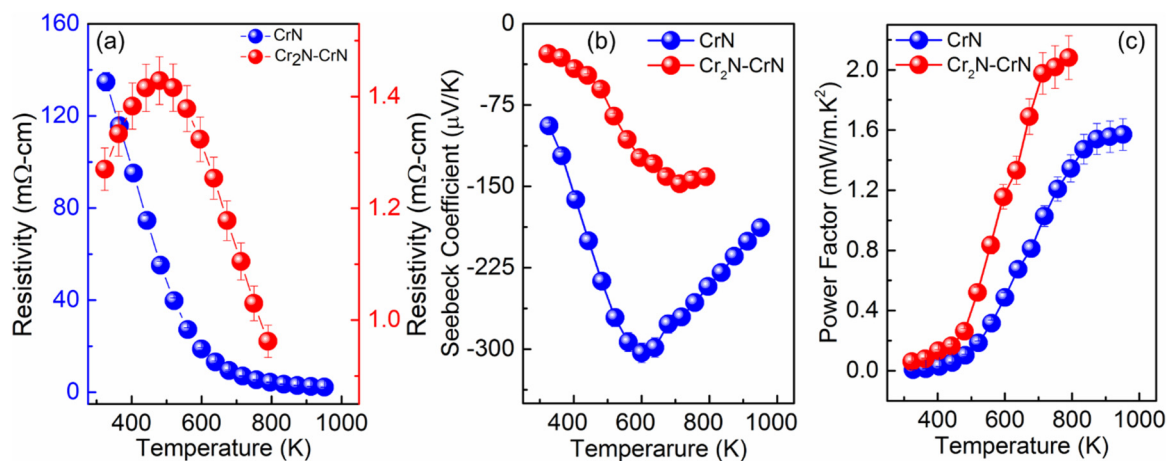


FIG. 4. (a) Temperature-dependent electrical resistivity of the phase-pure CrN and in-plane Cr₂N-CrN metal-semiconductor heterostructure is presented. Phase-pure CrN exhibits a clear Arrhenius-type thermal activation representative of its semiconducting nature. The in-plane Cr₂N-CrN heterostructure exhibits a barrier height of ~ 70 meV with carrier transport determined by thermionic emission and/or thermionic field emission processes. (b) Seebeck coefficient of CrN exhibits a V-shaped curve that is representative of its thermal-activation nature. The Cr₂N-CrN heterostructure shows an overall smaller Seebeck coefficient with a maximum at ~ 600 – 650 K. (c) The in-plane Cr₂N-CrN metal-semiconductor heterostructure exhibits an overall higher thermoelectric power factor compared to CrN due to its lower resistivity and suitable Seebeck coefficient.

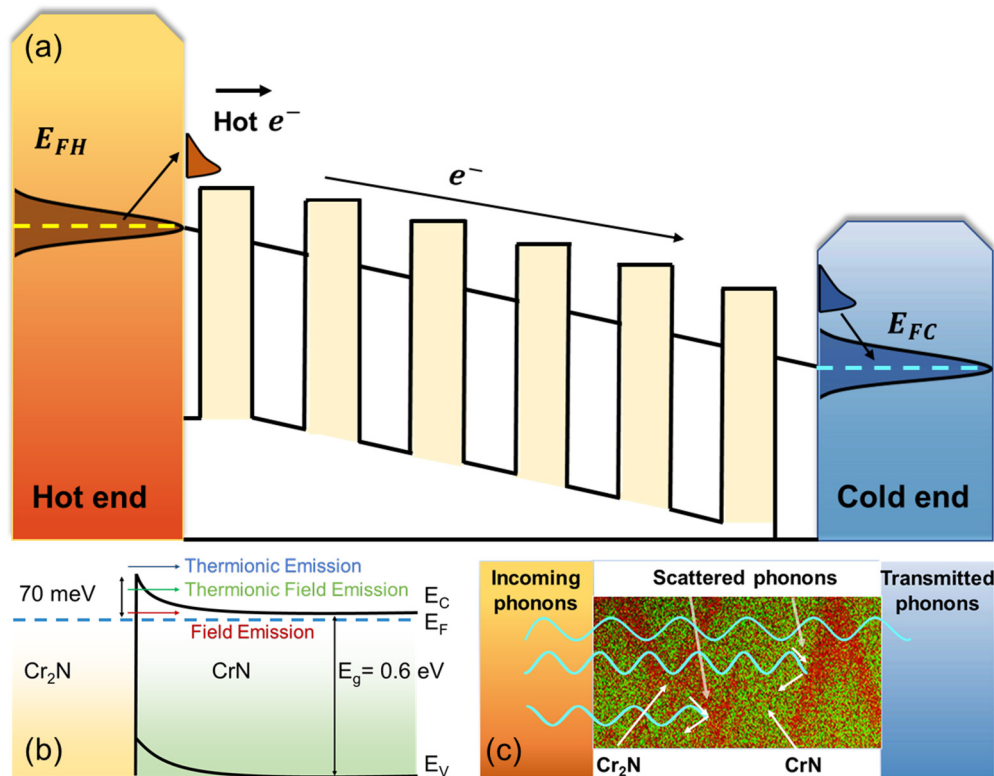


FIG. 5. (a) Schematic of electron conduction from hot-end to cold-end through the series of metal-semiconductor interfaces. Electrons from the hot end absorb thermal energy to cross the barrier at the metal-semiconductor interfaces and conduct through the heterostructure. (b) Schematic of Schottky barrier and different electron transport mechanisms across a single Cr_2N - CrN metal-semiconductor interface is presented. At high temperature (>500 K), electrons gain sufficient thermal energy to cross the Schottky barrier (70 meV) by means of thermionic emission and/or thermionic field emission. (c) Schematic of scattering of phonons in in-plane direction at the Cr_2N - CrN metal-semiconductor interface.

exhibits a Seebeck coefficient of $-27 \mu V/K$, which is about 3.5 times smaller than the Seebeck coefficient of phase-pure CrN . The Seebeck coefficient increases slowly from 300 to 500 K and faster after 500 K. The Seebeck coefficient nearly saturates around 680 K and then starts to decrease slightly at higher temperatures. Such behavior of the Seebeck coefficient is expected since the electrical resistivity never quite saturates within the measured temperature range. This observation, therefore, indicates that though the thermionic emission is quite prevalent in the Cr_2N - CrN heterostructure, a large number of carriers also undergo thermionic field emission whereby activated carriers can tunnel through the Schottky barrier at high temperature. Since semiconducting CrN exhibits a carrier concentration of $1.2 \times 10^{19} cm^{-3}$ at room temperature, the depletion width at the metal-semiconductor interface is expected to be rather moderate, which could facilitate the observed thermionic field emission process, which is also the case for a similar material scandium nitride (ScN) with carrier concentration $>10^{19} cm^{-3}$ [4]. Nevertheless, the in-plane Cr_2N - CrN metal-semiconductor heterostructure exhibits a high Seebeck coefficient of $\sim -150 \mu V/K$, which is smaller than that of phase-pure CrN but significantly higher than the Seebeck coefficient of metallic Cr_2N [65] (see SM for thermoelectric properties of Cr_2N [60]). The Seebeck coefficient value of the heterostructure is well suited for achieving a high thermoelectric power factor

and is comparable to the Seebeck coefficient of well-known thermoelectric materials such as ScN and Bi_2Te_3 [66,67].

The temperature-dependent thermoelectric power factor ($\frac{S^2}{\rho}$) [Fig. 4(c)] is calculated from the electrical resistivity and Seebeck coefficient. At low temperature, the power factor of phase-pure CrN is relatively low but above ~ 500 K the power factor value increases significantly with the increase in temperature and saturates to $\sim 1.6 mW/mK^2$ in the 850–900 K temperature range, which is comparable to the previous reports of maximum power factor in CrN [47,65,68]. With the onset of thermal activation behavior, the electrical resistivity is reduced drastically while a moderate Seebeck coefficient is maintained. As a result the power factor increases in the high temperature regime.

However, due to the two orders of magnitude lower resistivity and suitable Seebeck coefficients, the in-plane Cr_2N - CrN metal-semiconductor heterostructure exhibits a much higher power factor as compared to pure CrN over the entire measured temperature range. At ~ 780 K, a maximum power factor of $\sim 2.1 mW/mK^2$ is obtained for Cr_2N - CrN heterostructure, which amounts to $\sim 25\%$ increase with respect to phase-pure CrN . Such an improvement in the thermoelectric power factor is due to the drastic reduction in resistivity and formation of in-plane metal-semiconductor heterostructure, and the effect of Schottky barrier controlled carrier transport, which maintains a moderate Seebeck coeffi-

TABLE I. Thermoelectric power factor of well-known thermoelectric material in the similar temperature range.

Material	Temperature (K)	Power factor (mW/mK ²)
YbCd _{2-x} Zn _x Sb ₂ [71]	700	1.92
YbCd _{2-x} Mg _x Sb ₂ [72]	650	1.68
Eu(Zn _{1-x} Cd _x) ₂ Sb ₂ [73]	650	2.25
TiNiSn [74]	775	2.4
ScN [67]	550–600	2.3
TiFe _{0.15} Co _{0.85} Sb [75]	850	2.2
Mg ₃ Sb ₂ (Mn, Bi, Te) [76]	700	2
Hf _{0.44} Zr _{0.44} Ti _{0.12} CoSb _{0.8} Sn _{0.2} [77]	973	2.8

cient value. The measured power factor is comparable to the well-known nitride thermoelectric material ScN in the same temperature range. It also compares well with other well-established thermoelectric materials such as Bi₂Te₃, La₃Te₄ and undoped crystalline SiGe, etc. [66,69,70] (see Table I).

While the in-plane Cr₂N-CrN heterostructure exhibits a higher thermoelectric power factor compared to CrN, knowledge about the temperature-dependent thermal conductivity is necessary to determine its thermoelectric *Figure-of-merit* (zT) and to realize the full potential for waste-heat recovery applications. A time domain thermoreflectance technique with ~ 95 nm Al transducer is used to measure the thermal conductivity of the phase-pure CrN and the Cr₂N-CrN heterostructure along the cross-plane direction. Since CrN is homogeneous and isotropic, the cross-plane thermal conduction should resemble the heat flow along the in-plane direction. However, for the in-plane heterostructure, the cross-plane and in-plane thermal conduction are expected to be different since the inter-

faces are located along the in-plane direction predominantly. Unfortunately, the measurement of the in-plane thermal conductivity in heterostructures is extraordinarily challenging due to the high thermal conductivity of the MgO substrate (~ 42 W/mK) that draws heat down into the substrate preventing in-plane heat spreading in the film. Therefore, we rely on the cross-plane thermal conductivity of the CrN and the heterostructure to determine their potential for thermoelectric applications.

TDTR measurement shows [see Fig. 6(a)] that the thermal conductivity of the phase-pure CrN thin film increases with an increase in temperature from 300 to 700 K. At room-temperature (300 K), CrN exhibits a thermal conductivity of 3.42 W/mK, while at 700 K, the thermal conductivity is measured to be 4.69 W/mK, which amounts to about 37% increment. Since the electrical resistivity of CrN is quite high, the electronic contribution to the total thermal conductivity, determined by the Wiedemann-Franz law with in-plane electrical conductivity, as presented in Fig. 6(a), is quite small. Therefore, the increase in the thermal conductivity in CrN results almost entirely from lattice or phonon contributions. The increase in the lattice thermal conductivity as a function of temperature is quite anomalous given that in normal materials thermal conductivity at higher temperatures should decrease due to Umklapp scattering. For CrN, however, such enhancement of the thermal conductivity could be due to the anomalous phonon lifetime shortening in the high-temperature paramagnetic phase that is caused by spin-lattice coupling as described in a few recent theoretical and experimental studies [78,79]. Similar to CrN, the Cr₂N-CrN metal-semiconductor heterostructure exhibits an increase in cross-plane thermal conductivity with an increase in temperature. Since 87% of the heterostructure is composed of CrN, such an increase in the thermal conductivity is consistent with

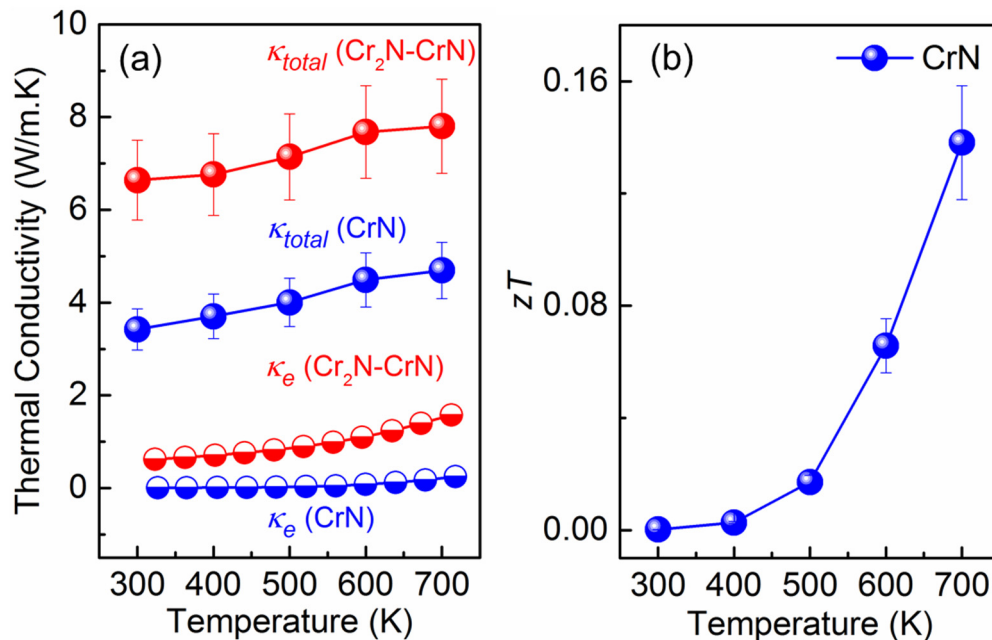


FIG. 6. (a) Cross-plane total thermal conductivity and electron contribution to the thermal conductivity of pure CrN and Cr₂N-CrN in-plane heterostructure. Contrary to the general behavior, the thermal conductivity of both pure CrN and Cr₂N-CrN in-plane heterostructure increases with temperature. (b) the thermoelectric *Figure-of-merit* (zT) of pure CrN is presented. At 700 K, CrN shows a maximum zT of 0.13.

pure CrN results. However, unlike CrN, the thermal conductivity is found to be a bit higher with a room temperature value of 6.64 W/mK which rises to 7.80 W/mK at 700 K. Since the metallic Cr₂N exhibits a room temperature thermal conductivity of 12.0 ± 1.8 W/mK [65], the measured room-temperature thermal conductivity of 6.7 W/mK is close to the volume-averaged mean value of the constituent materials.

With the knowledge of the power factor and thermal conductivity, the thermoelectric *Figure-of-merit* (zT) is calculated as a function of temperature. For the phase-pure CrN, zT increases with an increase in temperature and exhibits a maximum measured value of 0.13 at 700 K. Though the power factor of pure CrN saturates at the highest value around ~ 850 K, zT is reported only until 700 K due to the thermal conductivity measurement constraints at higher temperatures. Unlike CrN, determination of exact zT value for Cr₂N-CrN is not possible due to the anisotropy in the transport properties along the cross-plane and in-plane direction of the heterostructure. However, to have an idea about zT value of the heterostructure, we estimated the zT value assuming two possible scenarios (see SM for zT estimation of the heterostructure [60]).

IV. CONCLUSION

In conclusion, the growth of an epitaxial in-plane Cr₂N-CrN metal-semiconductor heterostructure is demonstrated which exhibits a higher thermoelectric power factor compared to both phase-pure rocksalt CrN and phase-pure metallic Cr₂N. The in-plane heterostructure is deposited on (001) MgO substrates by utilizing near equal negative formation enthalpy of nitridation for chromium (Cr) at el-

evated temperature, which results in the formation of a secondary hexagonal metallic Cr₂N phase in the semiconducting CrN matrix. The current transport along the in-plane direction is controlled by Schottky barrier heights at the metal-semiconductor interfaces exhibiting a barrier height of 70 meV. Due to the barrier controlled transport, electrical resistivity ranging between 1.0 and 1.4 m Ω cm and a Seebeck coefficient of ~ -150 μ V/K is achieved that leads to a high thermoelectric power factor of 2.1 mW/mK² at 780 K in the heterostructure. A TDTR method is used to determine the thermal conductivity of CrN and that of the heterostructure to estimate zT . These results mark a demonstration of an inorganic in-plane metal-semiconductor heterostructure and its improved thermoelectric properties.

ACKNOWLEDGMENTS

B.B., S.C., and B.S. acknowledge support from the International Centre for Materials Science and Sheikh Saqr Laboratory of the Jawaharlal Nehru Centre for Advanced Scientific Research. B.S. acknowledge the Young Scientist Research Award (YSRA) from the Board of Research in Nuclear Sciences (BRNS), Department of Atomic Energy (DAE), India, Grant No. 59/20/10/2020-BRNS/59020 for financial support. The authors acknowledge the instruments and scientific and technical assistance of Microscopy Australia at the Australian Centre for Microscopy and Microanalysis, The University of Sydney, a facility that is funded by the University, and State and Federal Governments.

The authors declare no conflict of interest.

-
- [1] G. D. Mahan, J. O. Sofo, and M. Bartkowiak, *J. Appl. Phys.* **83**, 4683 (1998).
 - [2] D. Vashaee and A. Shakouri, *Phys. Rev. Lett.* **92**, 106103 (2004).
 - [3] A. Shakouri, *Annu. Rev. Mater. Res.* **41**, 399 (2011).
 - [4] M. Garbrecht, I. McCarroll, L. Yang, V. Bhatia, B. Biswas, D. Rao, J. M. Cariney, and B. Saha, *J. Mater. Sci.* **55**, 1592 (2020).
 - [5] G. V. Naik, B. Saha, J. Liu, S. M. Saber, E. Stach, J. M. K. Irudayaraj, T. D. Sands, V. M. Shalaev, and A. Boltasseva, *Proc. Natl. Acad. Sci. USA* **111**, 7546 (2014).
 - [6] B. Saha, G. V. Naik, S. Saber, E. Stach, V. M. Shalaev, A. Boltasseva, and T. D. Sands, *Phys. Rev. B* **90**, 125420 (2014).
 - [7] M. Garbrecht, L. Hultman, M. H. Fawey, T. D. Sands, and B. Saha, *J. Mater. Sci.* **53**, 4001 (2018).
 - [8] Y. Guo, W. Newman, C. L. Cortes, and Z. Jacob, *Adv. Optoelectron.* **2012**, 452502 (2012).
 - [9] J. Liu and E. E. Narimanov, *Phys. Rev. B* **91**, 041403 (2015).
 - [10] Y. Guo and Z. Jacob, *Opt. Express* **21**, 15014 (2013).
 - [11] M. Sakhdari, M. Hazizadegan, and M. Farhat, *Nano Energy* **26**, 371 (2016).
 - [12] Y. Sivan and Y. Dubi, *Appl. Phys. Lett.* **117**, 130501 (2020).
 - [13] B. Saha, S. Saber, G. V. Naik, A. Boltasseva, E. Stach, E. P. Kvam, and T. D. Sands, *Phys. Status Solidi B* **252**, 251 (2015).
 - [14] B. Biswas, S. Nayak, V. Bhatia, A. I. K. Pillai, M. Garbrecht, M. H. Modi, M. Gupta, and B. Saha, *J. Vac. Sci. Technol. A* **38**, 053201 (2020).
 - [15] M. Garbrecht, J. L. Schroeder, L. Hultman, J. Birch, B. Saha, and T. D. Sands, *J. Mater. Sci.* **51**, 8250 (2016).
 - [16] J. F. O'Hara, J. Zide, A. Gossard, A. J. Taylor, and R. D. Averitt, *Appl. Phys. Lett.* **88**, 251119 (2006).
 - [17] A. K. Azad, R. P. Prasankumar, D. Talbayev, A. J. Taylor, R. D. Averitt, J. Zide, H. Lu, A. C. Gossard, and J. F. O'Hara, *Appl. Phys. Lett.* **93**, 121108 (2008).
 - [18] B. E. Tew, P. Vempati, L. E. Clinger, C. C. Bomberger, N. I. Halaszynski, T. Favaloro, J. H. Seol, J. P. Feser, A. Majumdar, A. Shakouri, J. E. Bowers, J. Bahk, and J. Zide, *Adv. Electron. Mater.* **5**, 1900015 (2019).
 - [19] L. D. Hicks and M. S. Dresselhaus, *Phys. Rev. B* **47**, 12727 (1993).
 - [20] S. V. Faleev and F. Leonard, *Phys. Rev. B* **77**, 214304 (2008).
 - [21] J. Zide, D. Vashaee, Z. X. Bian, G. Zeng, J. E. Bowers, A. Shakouri, and A. C. Gossard, *Phys. Rev. B* **74**, 205335 (2006).
 - [22] H. T. Chen, W. J. Padilla, J. Zide, A. C. Gossard, A. J. Taylor, and R. D. Averitt, *Nature (London)* **444**, 597 (2006).
 - [23] W. Kim, J. M. O. Zide, A. Gossard, D. Klenov, S. Stemmer, A. Shakouri, and A. Majumdar, *Phys. Rev. Lett.* **96**, 045901 (2006).

- [24] T. S. Basu, R. Yang, S. J. Thiagarajan, S. Ghosh, S. Gierlotka, and M. Ray, *Appl. Phys. Lett.* **103**, 8 (2013).
- [25] Q. Zhang, X. Ai, L. Wang, Y. Chang, W. Luo, W. Jiang, and L. Chen, *Adv. Funct. Mater.* **25**, 966 (2015).
- [26] B. Biswas and B. Saha, *Phys. Rev. Mater.* **3**, 020301 (2019).
- [27] M. S. Sander, R. Gronsky, T. Sands, and A. M. Stacky, *Chem. Mater.* **15**, 335 (2003).
- [28] S. A. Sapp, B. B. Lakshmi, and C. R. Martin, *Adv. Mater.* **11**, 402 (1999).
- [29] X. Duan, C. Wang, J. C. Shaw, R. Cheng, Y. Chen, H. Li, X. Wu, Y. Tang, Q. Zhang, A. Pan, J. Jiang, R. Yu, Y. Huang, and X. Duan, *Nat. Nanotechnol.* **9**, 1024 (2014).
- [30] J. Chen, W. Zhou, W. Tang, B. Tian, X. Zhou, H. Xu, Y. Liu, D. Geng, S. J. R. Tan, W. Fu, and K. P. Loh, *Chem. Mater.* **28**, 7194 (2016).
- [31] J. Wang, Z. Li, H. Chen, G. Deng, and X. Niu, *Nano-Micro Lett.* **11**, 48 (2019).
- [32] C. Wang, Two-dimensional semiconducting materials for next-generation electronics and optoelectronics, Ph.D. Thesis, University of California, Los Angeles, 2017.
- [33] D. R. Chen, M. Hofmann, H. M. Yao, S. K. Chiu, S. H. Chen, Y. R. Luo, C. C. Hsu, and Y. P. Hsieh, *ACS Appl. Mater. Interfaces.* **11**, 6384 (2019).
- [34] K. Ye, L. Liu, Y. Liu, A. Nie, K. Zhai, J. Xiang, B. Wang, F. Wen, C. Mu, Z. Zhao, Y. Gong, Z. Liu, and Y. Tian, *Adv. Optical Mater.* **7**, 1900815 (2019).
- [35] J. Zhang, W. Xie, J. Zhao, and S. Zhang, *2D Mater.* **4**, 015038 (2017).
- [36] M. Houssa, K. Iordanidou, A. Dabral, A. Lu, G. Pourtois, V. Afanasiev, and A. Stesmans, *ACS Appl. Nano Mater.* **2**, 760 (2019).
- [37] G. Berg, C. Friedrich, E. Broszeit, and C. Berger, *Surf. Coat. Technol.* **86-87**, 184 (1996).
- [38] J. A. Sue and T. P. Chang, *Surf. Coat. Technol.* **76-77**, 61 (1995).
- [39] M. Sikkens, A. A. M. T. V. Heereveld, E. Vogelzang, and C. A. Boose, *Thin Solid Films* **108**, 229 (1983).
- [40] P. Hones, N. Martin, M. Regula, and F. Lévy, *J. Phys. D* **36**, 1023 (2003).
- [41] M. Lackner, W. Waldhauser, L. Major, and M. Kot, *Coatings* **4**, 121 (2014).
- [42] J. D. Browne, P. R. Liddell, R. Street, and T. Mills, *Phys. Status Solidi A* **1**, 715 (1970).
- [43] L. M. Corliss, N. Elliott, and J. M. Hastings, *Phys. Rev.* **117**, 929 (1960).
- [44] R. M. Ibberson and R. Cywinski, *Physica B* **180-181**, 329 (1992).
- [45] M. E. McGahay, B. Wang, J. Shi, and D. Gall, *Phys. Rev. B* **101**, 205206 (2020).
- [46] C. X. Quintela, J. P. Podkaminer, M. N. Luckyanova, T. R. Paudel, E. L. Thies, D. A. Hillsberry, D. A. Tenne, E. Y. Tsybal, G. Chen, C. B. Eom, and F. Rivadulla, *Adv. Mater.* **27**, 3032 (2015).
- [47] S. Kerdsonpanya, B. Sun, F. Eriksson, J. Jensen, J. Lu, Y. K. Koh, N. V. Nong, B. Balke, B. Alling, and P. Eklund, *J. Appl. Phys.* **120**, 215103 (2016).
- [48] A. L. Febvrier, N. V. Nong, G. Abadias, and P. Eklund, *Appl. Phys. Express* **11**, 051003 (2018).
- [49] M. A. Gharavi, D. Gambino, A. Le. Febvrier, F. Eriksson, R. Armiento, B. Alling, and P. Eklund, *Mater. Today Commun.* **28**, 102493 (2021).
- [50] D. Gall, C.-S. Shin, R. T. Haasch, I. Petrov, and J. E. Greene, *J. Appl. Phys.* **91**, 5882 (2002).
- [51] M. A. Gharavi, G. Greczynski, F. Eriksson, J. Lu, B. Balke, D. Fournier, A. Le. Febvrier, C. Pallier, and P. Eklund, *J. Mater. Sci.* **54**, 1434 (2019).
- [52] L. Wang and R. D. Pehlke, *Metall. Trans. B* **19**, 471 (1988).
- [53] H. Ono-Nakazato, K. Taguchi, T. Usui, K. Tamura, and Y. Tomatsu, *Metall. Mater. Trans. B* **32**, 1113 (2001).
- [54] B. Biswas, S. Chakraborty, A. Joseph, S. Acharya, A. I. K. Pillai, C. Narayana, V. Bhatia, M. Garbrecht, and B. Saha, Secondary phase limited metal-insulator phase transition in chromium nitride thin films (unpublished).
- [55] D. G. Cahill, *Rev. Sci. Instrum.* **75**, 5119 (2014).
- [56] K. Kang, Y. K. Koh, C. Chiritescu, X. Zheng, and D. G. Cahill, *Rev. Sci. Instrum.* **79**, 114901 (2008).
- [57] J. P. Feser and D. G. Cahill, *Rev. Sci. Instrum.* **83**, 104901 (2012).
- [58] R. M. Costescu, M. A. Wall, and D. G. Cahill, *Phys. Rev. B* **67**, 054302 (2003).
- [59] Y. K. Koh, S. L. Singer, W. Kim, J. M. O. Zide, H. Lu, D. G. Cahill, A. Majumdar, and A. C. Gossard, *J. Appl. Phys.* **105**, 054303 (2009).
- [60] See Supplemental Material at <http://link.aps.org/supplemental/10.1103/PhysRevMaterials.5.114605> for additional details about experimental methods, Arrhenius activation energy calculation, thermoelectric properties of CrN-Cr₂N heterostructure with large Cr₂N and zT calculations.
- [61] J. Roberson, *Phys. Status Solidi A* **207**, 261 (2010).
- [62] F. Leonard and A. A. Talin, *Nat. Nanotechnol.* **6**, 773 (2011).
- [63] M. G. Kanatzidis, S. D. Mahanti, and T. P. Hogan, *Chemistry, Physics, and Materials Science of Thermoelectric Materials: Beyond Bismuth Telluride* (Springer Science & Business Media, New York, 2003).
- [64] N. S. Kini, A. M. Srydom, H. S. Jeevan, C. Geibel, and S. Ramakrishnan, *J. Phys.: Condens. Matter* **18**, 8205 (2006).
- [65] M. N. Gharavi, S. Kerdsonpanya, S. Schmidt, F. Eriksson, N. V. Nong, Jun Lu, B. Balke, D. Fournier, L. Belliard, A. Le. Febvrier, C. Pallier, and P. Eklund, *J. Phys. D* **51**, 355302 (2018).
- [66] M. Saleemi, M. S. Toprak, S. Li, M. Johnsson, and M. Muhammed, *J. Mater. Chem.* **22**, 725 (2012).
- [67] D. Rao, B. Biswas, E. Flores, A. Chatterjee, M. Garbrecht, Y. R. Koh, V. Bhatia, A. I. K. Pillai, P. E. Hopkins, M. M. Gonzalez, and B. Saha, *Appl. Phys. Lett.* **116**, 152103 (2020).
- [68] P. Eklund, S. Kerdsonpanya, and B. Alling, *J. Mater. Chem. C* **4**, 3905 (2016).
- [69] H. Takiguchi, A. Matoba, K. Sasaki, Y. Okamoto, H. Miyazaki, and J. Morimoto, *Mater. Trans.* **51**, 878 (2010).
- [70] H. L. Gao, T. J. Zhu, H. Wang, Z. F. Ren, and X. B. Zhao, *J. Phys. D* **45**, 185303 (2012).
- [71] X. J. Wang, M. B. Tang, H. Chen, H. Chen, X. X. Yang, J. T. Zhao, U. Burkhardt, and Y. Grin, *Appl. Phys. Lett.* **94**, 092106 (2009).

- [72] Q. Cao, J. Zheng, K. Zhang, and G. Ma, *J. Alloy. Compd.* **680**, 278 (2016).
- [73] H. Zhang, M. Baitinger, M. B. Tang, Z. Y. Man, H. H. Chen, X. X. Yang, Y. Liu, L. Chen, Y. Grin, and J. T. Zhao, *Dalton Trans.* **39**, 1101 (2010).
- [74] H. Muta, T. Kanemitsu, K. Kurosaki, and S. Yamanaka, *J. Alloy. Compd.* **469**, 50 (2009).
- [75] T. Wu, W. Jiang, X. Li, Y. Zhou, and L. Chen, *J. Appl. Phys.* **102**, 103705 (2007).
- [76] X. Chen, H. Wu, J. Cui, Y. Xiao, Y. Zhang, J. He, Y. Chen, J. Cao, and W. Cai, *Nano Energy* **52**, 246 (2018).
- [77] R. He, H. S. Kim, Y. Lan, D. Wang, S. Chen, and Z. Ren, *RSC Adv.* **4**, 64711 (2015).
- [78] I. Stockem, A. Bergman, A. Glensk, T. Hickel, F. Kormann, B. Graboswki, J. Neugebauer, and B. Alling, *Phys. Rev. Lett.* **121**, 125902 (2018).
- [79] O. Jankovský, D. Sedmidubský, Š. Huber, P. Šimek, and Z. Sofer, *J. Eur. Ceram. Soc.* **34**, 4131 (2014).